Science Advances
AAAS

Supplementary Materials for

Multistable shape programming of variable-stiffness electromagnetic devices

Bekir Aksoy and Herbert Shea

Corresponding author: Herbert Shea, herbert.shea@epfl.ch

Sci. Adv. **8**, eabk0543 (2022)
DOI: 10.1126/sciadv.abk0543

The PDF file includes:

Supplementary Text
Figs. S1 to S13
Tables S1 and S2
Legends for movies S1 and S2

Other Supplementary Material for this manuscript includes the following:

Movies S1 and S2

Supplementary Text

Design overview of the joints and segments

The beam is designed with narrow and wide sections. The wide section allows high number of turns of the liquid metal coils to produce high electromagnetic forces. The narrow sections, on the other hand, are designed to undergo very large bending and twisting deformations.

The overall design parameters of the joints, segments, and coils are shown in Fig. S1. The joints have the same length of 5 mm but their widths vary from 4 mm to 4.5 mm.

Thermoplastic shape memory polymers (SMP)

We used thermoplastic shape memory polyurethane (MM7520 from SMP technologies) as the variable stiffness material. This material enabled us to tune the stiffness of the device by changing its temperature. It also has shape memory effect which allowed us to fix the deformation into place.

A dynamic mechanical analyzer (DMA Q800 from T.A. Instruments) was used to measure thermomechanical behavior of the SMP. The DMA tests were carried out in the tensile mode with a strain amplitude of 0.1%. The temperature was swept from 0 °C to 140 °C with a ramp of 3 °C/min. Figure S2 shows the storage (Y') and loss modulus (Y''), and loss factor tan(delta) plotted as functions of the temperature. When the temperature is swept from 20 °C to 90 °C, the modulus of the SMP reduces more than 100 times.

Temperature dependency of the torsional and bending stiffness of the joints

As seen from Fig. S3, the Young's modulus of the SMP strongly depends on the temperature, therefore we used the measured Young's modulus of the MM7520 in the simulations. Although the Young's modulus of the PDMS layer also depends on the temperature, this dependency is small compared to the SMP and we assume it is constant.

Figure S3 shows the computed bending and torsional stiffness of three joints as functions of the temperature. The bending and torsional stiffness of the joints as functions of the temperature was computed using COMSOL Multiphysics. As the temperature increases above the glass transition temperature, the stiffness of all joints drops sharply. Due to small variation in their widths, there is a difference among their bending stiffness. The computed torsional stiffness of the joints is shown in Fig. S3C. Similar to the trend observed in the bending stiffness, the torsional stiffness drops by a factor of 27 when the temperature is swept from the room temperature to above 90 °C. In this section, the stiffness calculation is carried out for the predefined layer thickness: the SMP layers has a thickness of 60 µm and the thickness of the PDMS is 1.30 mm. The following section details the optimization procedure of the SMP thickness.

Working principle of multistable variable stiffness electromagnetic actuators

The variable stiffness beam is composed of three wide sections called segments, three narrow regions (joints), and one clamping section. The clamping section houses the electrical connections to the liquid-metal (LM) coils and to the Joule heaters. During the experiments, the device is clamped from this section. The segments are the wide sections of the device with a surface area of 15 mm x 15 mm and the liquid-metal coils are embedded here (see Fig. S1). The electromagnetic forces and torques are produced in these sections. The joints are the narrow parts of the device, with varying widths from 4 mm to 4.5 mm. During actuation, the target joints are softened by the stretchable Joule heaters where they undergo either bending or twisting deformation.

The device consists of multiple layers of silicone (PDMS), shape memory polymer, and polyurethane based stretchable heaters. The silicone layer has microfluidic channels that are filled with eutectic gallium-indium (EGaIn). This layer is sandwiched between two SMPs, proving as composite structure with variable stiffness material on the outer sides. These SMP layers are used as the variable stiffness material and also as the latching element. Each joint has a pair of heating electrodes placed on the both sides. They are made of the same materials as the SMPs but are mixed with carbon particles (EC-600JD from Akzo Nobel N.V.). They are used to reduce the stiffness of the SMP layers by increasing the SMP temperature above the glass transition temperature (T_g). The heaters are designed for the localized heating of the joint sections only. When the device is actuated, only the soft (activated) joints deform. The segments and the unaddressed joints do not deform during the actuation as they are one order of the magnitude stiffer.

During actuation, the soft joint undergoes either torsional or bending deformation depending on the relative direction of magnetic field with respect to liquid-metal coils. Two deformation types are schematically represented in Fig. S4. If the magnetic field is parallel to the surface normal of the segment, the generated electromagnetic force is parallel to the magnetic field lines (see force component at $\theta=0$ in Fig. S5 and more details are in the modeling section). Therefore, the joint bends when a current is applied to the liquid-metal coil. Flipping the direction of the LM current still generates a bending motion but in the opposite direction. This way, the antagonistic motion can be easily achieved in these electromagnetic actuators by just reversing the polarity of the LM current. If the magnetic field is perpendicular to the surface normal and in the lateral direction as shown in Fig. S4B, applying current to the liquid metal coils generates Lorentz forces in the upper and lower segments of the liquid-metal coils. Due to direction of the current in the coil segments, the electromagnetic force acts in the opposite directions in the upper and lower parts. This creates a torque and twists the soft joint. Reversing the polarity of the LM current generates a torsional deformation in the opposite direction.

Thermal limitation of the LM current on the shape fixation of the SMP

As explained in the previous section, the device deforms through its soft joint where the joint softened by the heaters. However, the current of the liquid-metal channel also generates heat in the segment and this heat transfers to the adjacent joint. When the liquid-metal coil is actuated with a current of I_{LM}, it produces Joule heating

$$P_{LM} = I_{LM}^2 R_{LM} \tag{1}$$

where I_{LM} is the current passing through liquid-metal coil and R_{LM} is the electrical resistance of the coil. Most of this resistive heating dissipates to the air through convection but a portion it transfers to the adjacent joint by conduction.

During the actuation, this heat transfer can be used as a secondary heating source for the softening the joint. As seen in this specific scenario, the cross-heating can be useful if we need to heat the adjacent joint. However, this only applies to the actuation state and in the latching step this cross-heating has an adverse effect. In order to lock the deformed shape, the joint needs to be cooled down (ideally down to room temperature). In the latching process, the heaters are turned off while the LM current is still on. If the heating and LM currents were simultaneously removed, the device would immediately go back to its undeformed state and the latching wouldn't be possible. If the cross-heating between the actuated segment and the joints is too high during the latching process, the deformation cannot be locked with high fixation ratio.

Temperature effect of the LMC current on the choice of SMP material

As previously discussed, the LM current produces resistive heat and this transfers to the joints through conduction. At high current, this becomes crucial as it increases the joint temperature during the latching which adversely affects the latching performance. Figure S6 depicts the relationship between the electromagnetic force generated in a segment and the temperature of its adjacent joint as functions of the LM current. Figure S6A shows the schematic of the segments and joints. The electromagnetic force generated in the segment is linearly proportional to the LM current whereas the joint temperature is proportional to the square of this current ($\propto I_{LM}^2 R_{LM}$).

The glassy and rubbery regions of a thermo-responsive SMP are schematically presented on the force and temperature graph in Figure S6B. The SMP is stiff in the glassy region and becomes very soft in the rubbery state. For a given SMP material, the temperature of the joint needs to be kept below the glass transition temperature to allow a good latching. Therefore, the maximum current that we can put in the LM is limited by the T_g of the chosen SMP material. The device can be operated at any LM current that allows a latching temperature below the glass transition temperature ($T<T_g$).

Although the latching is very good at low LM current, the actuation deformation is small due to low electromagnetic force. At high LM current, on the other hand, large deformations can be achieved. However, due to elevated latching temperature at this LM current range, the shape fixation is poor. Using SMP materials with higher T_g allows higher LMC current and eventually high force and large deformation. However, using very high T_g SMP requires more heating power and increases the actuation and latching time.

The selection of the SMP is exemplified with two specific SMP materials, namely MM4520 and MM7520 (both are from SMP technologies). Both are thermoplastic polyurethanes with glass transition temperatures around 45 °C and 75 °C. Figure S7 shows the dynamic mechanical analysis of these materials. The DMA tests were carried out in the tensile mode with a strain amplitude of 0.1%. The temperature was swept from 0 °C to 120 °C with a ramp of 3 °C/min. The DMA results show that both materials are very stiff at room temperature with Young's moduli above >1 GPa. As the temperature increases above T > 45 °C, the stiffness of the MM4520 drastically decreases while theMM7520 maintains its stiff structure until 80 °C. Increasing the temperature further above 80 °C sharply decreases the rigidity of the MM7520.

The glass transition of the SMP material plays a crucial role in both actuation and latching steps. To achieve large deformation during the actuation, the SMP needs to be softened in order to reduce their stiffening effect. To fix the actuation deformation, the SMP layers need to be cooled down below their glass transition temperature; the lower the SMP temperature the better latching. Since the LM current is on during the latching process, the temperature of the joint is higher than room temperature due to the cross-heating between the segment and the joint. In order to lock the actuation deformation, the joint's temperature needs to be lower than the glass transition temperature of the SMP. Using high T_g SMP allows us to operate at higher latching temperature. The Young's modulus-temperature graphs in Figure S7B shows how much these materials can resist the temperature change before getting soft. This enables us to choose the suitable SMP materials for the desired applications.

To investigate how much force we can achieve in a segment before softening the adjacent joint, we used a finite element model (FEM) for the thermal analysis and a numerical model for the computation of the electromagnetic force. COMSOL software was used to compute the temperature of the joint as a function of the liquid-metal current. The geometry of the device was first constructed in the software and the proper parameters were assigned to the materials. As we considered the heat generation in the EGaIn channels and the heat transfer between the materials and air (conduction and convection), we needed the thermal conductivity, heat capacity, and density of the materials, and electrical conductivity of EGaIn and heaters (see **Table S1**). Although the other materials parameters, e.g., the Young's moduli and Poisson's ratio, needed to run the simulation in COMSOL, they didn't affect the thermal analysis. The heat produced in the LM coil transfers to the other sections of the device through conduction and also dissipates to the air through convection.

Table S1. Material parameters required for thermal analysis in FEM simulations

Parameter	Unit	SMP	PDMS	EGaIn	Heater
Thermal conductivity	$Wm^{-1}K^{-1}$	0.17	0.15	26.4	1.6
Electrical conductivity	Sm^{-1}	-	-	$3.4x10^6$	0.644
Heat capacity	$Jkg^{-1}K^{-1}$	1260	1460	305	1260
Density	kgm^{-3}	1210	970	6250	960

In the simulations, the LM current of the furthest segment was swept from 0 A to 2 A with an increment of 0.1 A and the temperature of its adjacent joint was computed (see schematic in Fig. 7SB). The surface plot shows the temperature distribution in the device at $I_{LM} = 1.5\ A$. The blue curve shows how the joint temperature evolves as the LM current increases. The joint temperature is correlated to the heating power of the LM, which is proportional to the square of the current and the electrical resistance of the LM ($\propto I_{LM}^2 R_{LM}$).

To compute the interaction force between coaxial magnet and liquid-metal coil (no deformation), we can assume them as two magnetic dipoles with one being the dipole of the plate magnet and the other one being the magnetic moment of the coils. The following section includes the details of this force calculation. The interaction force between the plate magnet and the LM is plotted on the joint temperature vs. LM current graph. The graph can be interpreted for MM7520 and MM4520 materials. As MM4520 gets soft at relatively lower temperature, the maximum electromagnetic force of this materials is around 30 mN. MM7520 which allows operations at higher LM current as it has high T_g and can achieve higher electromagnetic force before softening, e.g. 55 mN. We therefore chose MM7520 as our SMP material in this study.

Modeling multi-stable electromagnetic devices for large deformation and high stiffness

This section details the model we developed for the multistable electromagnetic actuators. First, we drive the equations for the actuation and latched deformation of the devices in the twisting mode. Then we follow the same procedure for the bending deformation.

The torsional deformation of a soft joint is demonstrated in Fig. S4. The liquid-metal coils are placed in a magnetic field that is perpendicular to the surface normal of the segment. When the current of these coils is switched on, the Lorentz forces is produced. The cross-sections of the device segment at the initial and the deformed states are shown in Fig. S4A. The initial distance between the coil segment and the magnet are represented with z_i with i being the number of i^{th} coil segment. When the device is twisted with a LM current of I, the distance between the coil segments and the magnet changes (see actuated state in Fig. S4A). The distance in the deformed state is shown with z_i'. Due to the direction of the current in the coil segments, the Lorentz forces act in the opposite directions. As seen from the schematics, the Lorentz force on the left-hand side of the coil is downward whereas on the right-hand side of the coil the force acts in the upward direction. This creates a torque on the joint which can be quantified as:

$$T = \sum B_{z(z_i')} I L_i d_i' \qquad (1)$$

where $B_{z(z_i')}$ is the magnetic field in the *z* direction at distance of z_i', I is the LM current, L_i is the length of the coil segment, d_i' is the distance between the coil segment and the center of the rotation. Here, we see that z_i and d_i depend on the angle of the twist (θ_t). The general formula of the twisting angle for the actuation can be written as:

$$\theta_t = \frac{TL_{joint}}{<GJ>} = \sum B_{z(z_i')} I L_i d_i' \frac{L_{joint}}{<GJ>} \qquad (2)$$

where $< GJ >$ is the equivalent torsional rigidity of the joint and $d_i' = d_i \cos(\theta_t)$ and $z_i' = z_i + d_i\big(1 - \cos(\theta_t)\big)$. z and z' are the distances between the magnet and coil segment before and after torsion. d and d' are the perpendicular distance between the Lorentz force of the coil segment and the center of the rotation before and after torsion. The equivalent torsional rigidity of the composite (SMP + PDMS + SMP) joints can be calculated as:

$$< GJ > = \frac{Y_{pdms}}{3}\left(\frac{wt_{pdms}^3}{12} + \frac{w^3 t_{pdms}}{12}\right) + \frac{Y_{smp}}{3}\left(\frac{w\left(\left(2t_{smp}+t_{pdms}\right)^3 - t_{pdms}^3\right)}{12} + \frac{2w^3 t_{smp}}{12}\right) \qquad (3)$$

where *Y* is the Young's modulus, w is the width of the joints, and *t* is the thickness of the layers. Once the actuation is achieved, the deformation is fixed by the SMP layers whereas the silicone (PDMS) layer wants to recovery its undeformed state. Then there exists a mechanical equilibrium between the SMP and silicone layers. The equation of the torque equilibrium for the final latched state can be written as:

$$\frac{\theta_{latch} G_{pdms} J_{pdms}}{L_{joint}} = \frac{(\theta_{actuation} - \theta_{latch}) G_{smp} J_{smp}}{L_{joint}} \qquad (4)$$

where θ_{latch} is the angle of the twist in the final state. Recall that, since the SMP layer already fixes its actuation deformation during the shape fixing step, the angle of the twist for this layer is $\theta_{actuated} - \theta_{latch}$ (not θ_{latch}). Isolating θ_{latch} from equation, we find:

$$\theta_{latch} = \frac{G_{smp} J_{smp}}{G_{smp} J_{smp} + G_{pdms} J_{pdms}} \theta_{act} \qquad (5)$$

We can follow the same procedure to find the bending angle of the joints in the actuation and latched states. Figure S4B shows the bending of the soft joint when actuated in a magnetic field parallel to the surface normal. Analytically calculating the attraction force between the magnet and liquid-metal coil in the bending configuration is, however, not as simple as in the twisting scenario. We, therefore, used a finite element model (COMSOL software). The geometry of the device is constructed in the software as shown in Supplementary Fig. 5A. The parameters used in this simulation are listed in Table S2.

During actuation, the segment either moves away from the magnet or approaches the magnet (see Fig. S4b). When the segment moves away, the distance between the magnet and the LM coils increases and vice versa. In both cases, the angle between the segment's surface normal and axial direction of the magnet changes, from 0 (undeformed state) to θ_{act}. Figure 5SB shows the components of the electromagnetic force as a function of θ_{act}.

In the undeformed (initial) position, only one component of the electromagnetic force (F_z) generates bending deformation. As the segment deforms, the F_y component also contributes to bending. F_x is almost zero for all angles, and it does not cause any bending. The total force that creates bending is

$$F_{bend(\theta)} = \sqrt{F_z^2 + F_y^2} \qquad (6)$$

F_{bend} is always in the direction of the surface normal of the segment. Knowing this electromagnetic force (acting on the center of the actuated segment) and using the beam deflection formula, we can compute the tip deflection of the joints in the actuation state as:

$$\theta_{act} = \frac{F_{bend} L_{joint}\left(L_{joint} + L_{segment}\right)}{2\left(Y_{pdms} I_{pdms} + Y_{smp} I_{smp}\right)} \qquad (7)$$

where Y and I are the Young's modulus and the area moment of inertia of the corresponding material. The subscript *act* stands for actuation. Here, we assume that the force acts on the center of the segment and only the joint section deforms. Knowing the tip deflection angle in the actuated state, we can find the strain in the cross-section as:

$$\epsilon_{act} = \frac{r - r_{act}}{\rho_{act}} \qquad (8)$$

where r and ρ are the neutral axis and the radius of the curvature, respectively. The subscripts *act* is used to differentiate the terms used in the actuated and latched states. To find the latched deformation, we follow the same procedure as we did for the torsional deformation. Once the bending deformation is achieved, we cool down the joint, allowing the SMP layers to fix the deformation. When latched, the PDMS tries to go back to its undeformed configuration whereas the SMP resist this recovery. The beam latches in a deformed state with a new radius of the curvatures (ρ_{latch}) and a neutral axis (r_{latch}). Therefore, there exists a balance of the moments between the SMP and PDMS layers. This can be written as follow using the Stoney's equation (39):

$$\int_{A_{pdms}} -Y_{pdms} \epsilon_{latch} r dA = \int_{A_{smp}} -Y_{smp} \frac{\epsilon_{latch} - \epsilon_{act}}{1 + \epsilon_{act}} r dA = 0 \qquad (9)$$

where $\varepsilon_{act} = (r - r_{act})/\rho_{act}$ and $\varepsilon_{latch} = (r - r_{latch})/\rho_{latch}$ and they correspond to the strains at the actuation and the latched states, respectively. A_{smp} and A_{pdms} stand for the cross-section areas of the SMP and PDMS layers. As we can see from this equation, the stress in the PDMS depends on its instant strain whereas the stress in the SMP depends not only on their instant strain but also the strain at which it fixes its deformation (38). We know that the neutral axis locates at the center of the device thickness ($r_{act} = r_{lact} = total\ thickness/2$) due to symmetrical structure and pure bending configuration. We also know that $\rho_{act} = L_{joint}/\theta_{act}$. Therefore, equation 10 is sufficient to find the latched deformation.

Table S2. Parameters used in the electromagnetic force calculation

Parameter	Value
Permanent magnetization	1×10^{6} Am^{-1}
Radius and height of the magnet	35 mm and 35 mm
Magnetic permeability	1.26×10^{-6} Nm^{-2}
Number of turns	3
Coil current	2 A
Distance between magnet and coil	15 mm
Mean radius of LM coils	12 mm

Characterization of the plate magnet

We used a plate magnet in our experiment. This simplified the experimental setup while providing high magnetic field. The magnetic field of the magnet was measured using a Teslameter (see Fig. S8). The sensor probe was placed on a XYZ motorized state and the magnetic fields in the radial and axial directions were measured as the stage was moved in the x, y, z directions. Figure S8B-C shows the measured magnetic field in the axial and radial directions as a function of the radial distance for different height. On the surface very closed to the magnet, the magnetic field is around 400mT and decreases as the height increases. During the experiments the device were placed close to the magnet to benefit from the high magnetic field.

Supplementary Figures

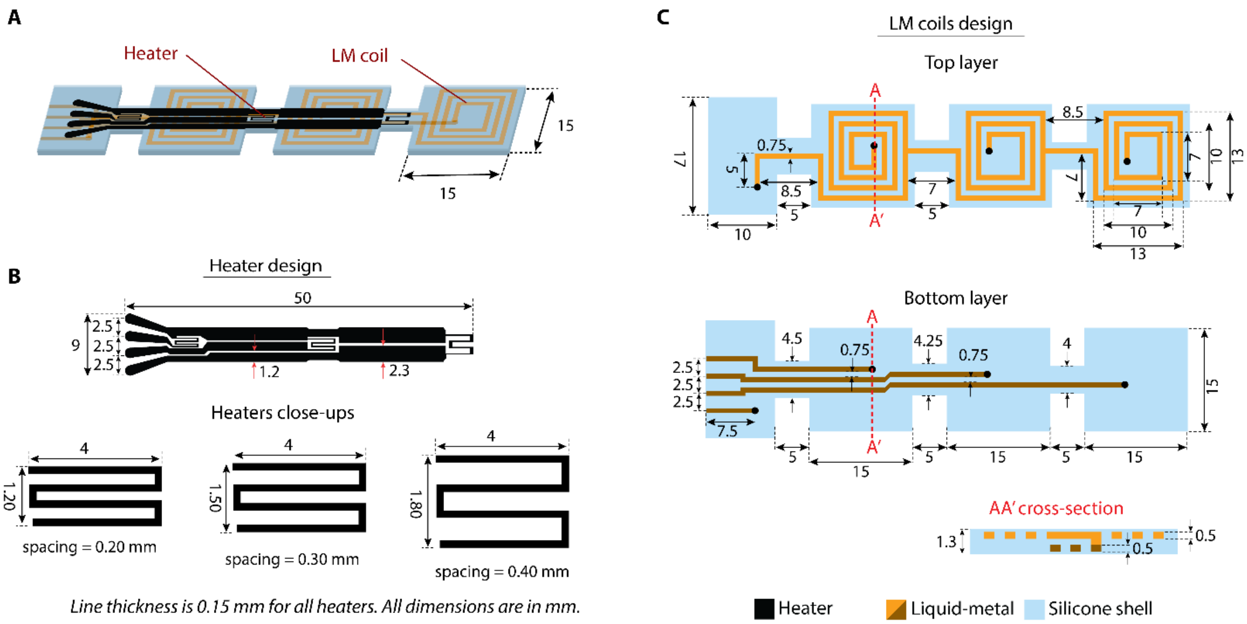

Line thickness is 0.15 mm for all heaters. All dimensions are in mm.

Fig. S1. Design parameters of the segments, heaters, joints, and liquid-metal coils. (A) Perspective view of the device showing the overall structure design and dimensions of the segments. (**B**) The dimensions of the heaters and conductive traces, and the close-up of each heater. (**C**) The design and dimensions of the liquid-metal coils.

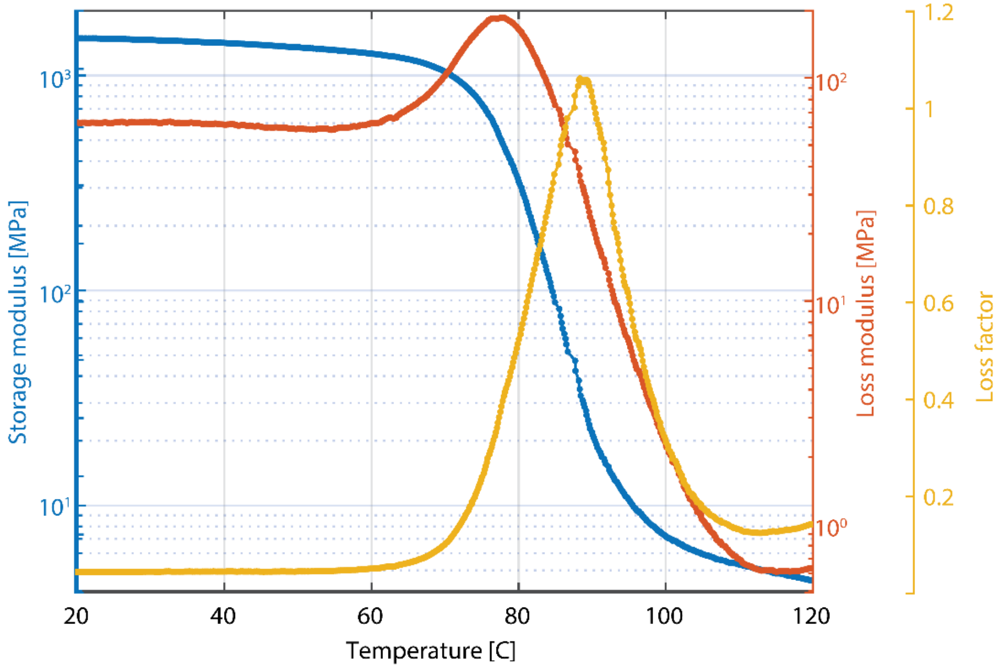

Fig. S2. Dynamic mechanical analysis of shape memory polymer. The storage (Y') and loss modulus (Y''), and loss factor tan(delta) of the SMP (MM7520 from SMP technologies) are plotted as functions of the temperature. When the temperature is swept from 20 °C to 90 °C, the modulus of the SMP reduces more than 100 times.

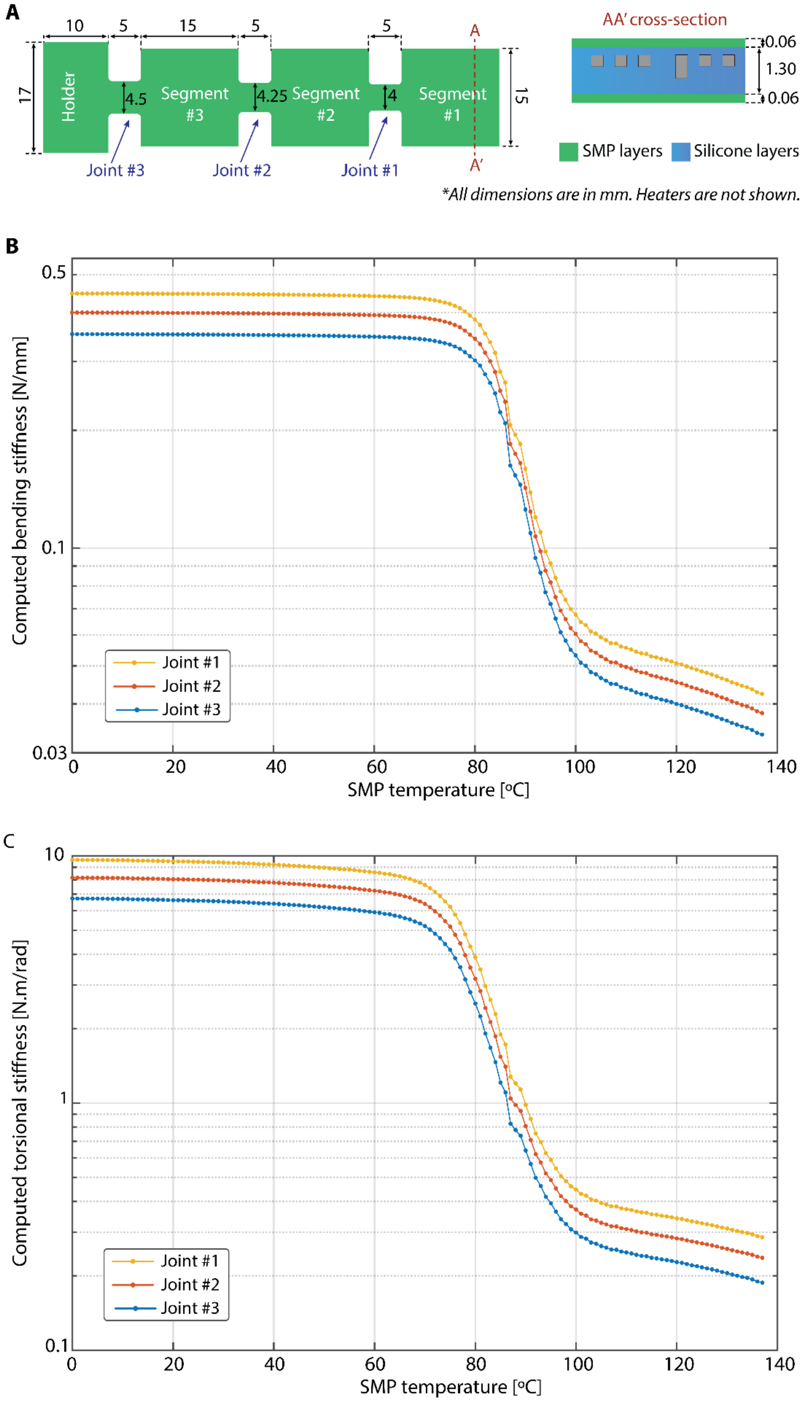

Fig. S3. The joints design and their bending and torsional stiffness at different temperatures. (**A**) The soft electromagnetic beam is composed of three identical segments housing the liquid metal coils and three joints acting as mechanical connectors between the segments. The segments are dimensionally identical with a surface area of *15 mm x 15 mm*. The joints have the same length of 5 mm but varying widths. The joints are designed as narrow as possible while accommodating their dedicated heater and the leads of the heaters. As the joints have different number of leads (electrical connections for the other joints), they have small width variations, changing from 4 mm to 4.5 mm. (**B-C**) The bending and the torsional stiffness of the joints as functions of the temperature. Both the bending and the torsional stiffness of the joints decrease significantly when the temperature increased above 80 °C. The variation in the widths of the joints causes a stiffness difference: the wider joints have higher stiffness.

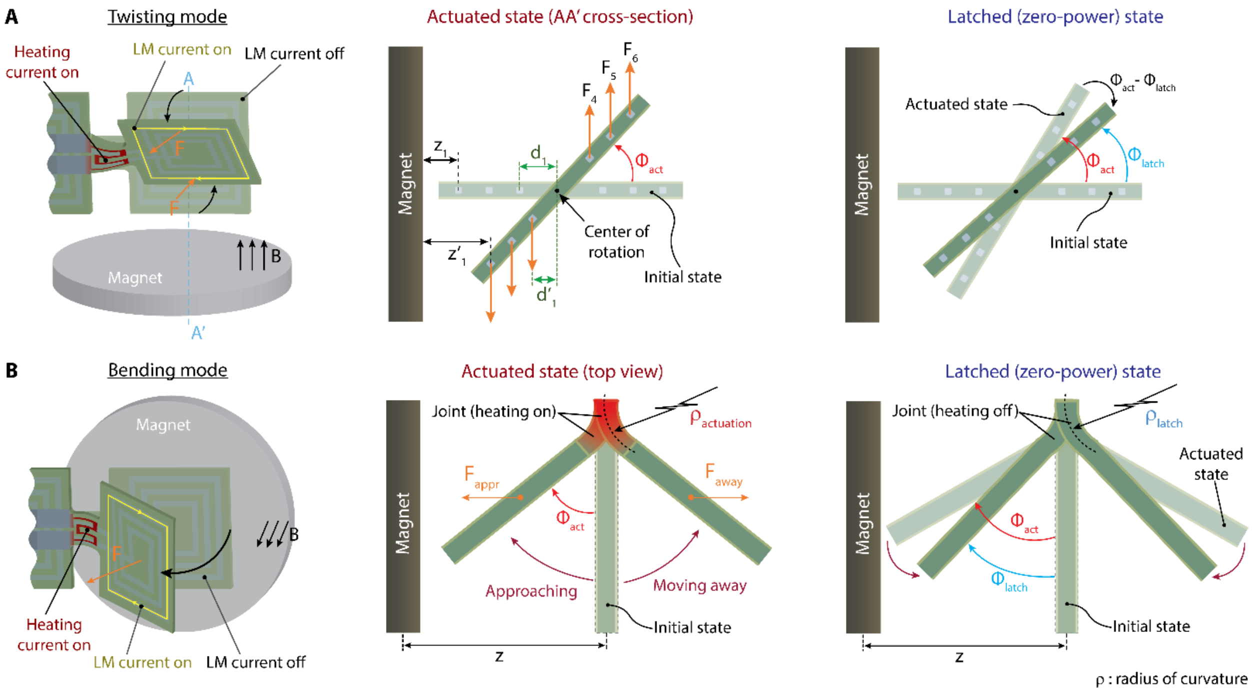

Fig. S4. The working principle of the variable stiffness electromagnetic beam and the calculation of the electromagnetic forces. (**A**) The schematics demonstrate the torsional deformation of the soft joint and the rotation of the adjacent segment when the LM current is switched on in a magnetic field that is perpendicular to the surface normal. AA' cross-section views of the segment show the configurations before and after the twisting. During twisting, the LM segments that are closed to the magnet (z_1, z_2, and z_3) move away from it whereas the far-away LM segments approach to the magnet. The Lorentz forces produced in these liquid-metal coil segments are in the opposite directions. This creates a torque and twists the joint. (**B**) The schematic shows the bending of the soft joints when the LM current is on in a magnetic field parallel to the surface normal. When the joint is bent, the corresponding segment either approaches to the magnet or moves away from it. The electromagnetic force acting on the LM is higher when approaching to the magnet than when it moves away from the magnet.

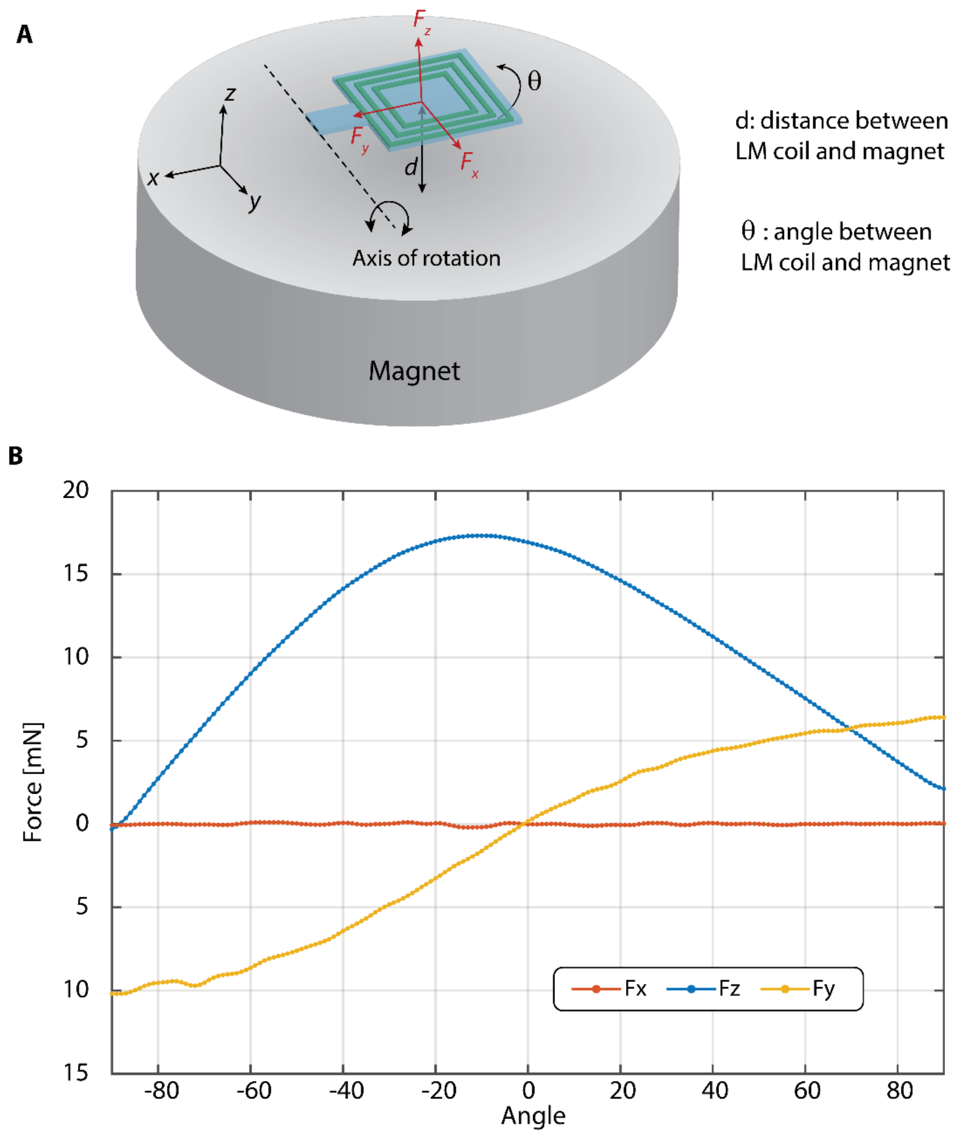

Fig. S5. The electromagnetic force between the liquid-metal coils and the permanent magnet obtained from finite element modeling. (**A**) The constructed geometry in COMSOL for force analysis. (**B**) The three components of the interaction force between the magnet and the LM coils are plotted as a function of the deflection angle of the segment. When the segment moves in the $+\theta$ direction, it moves away from the magnet.

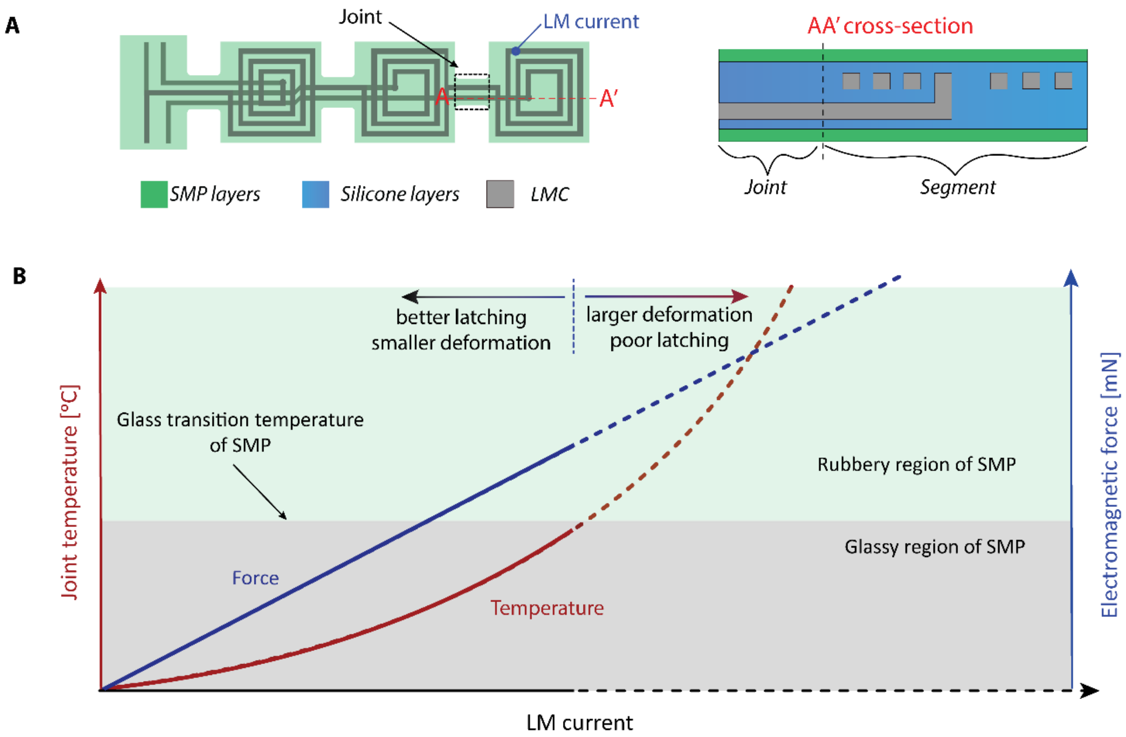

Fig. S6. Thermal limitation of the LM current on the choice of SMP material. (**A-B**) Due to non-zero electrical resistance of liquid-metal coils, heat is produced when the current is on and a portion of the produced heat transfers to the adjacent joint by conduction. During the latching process, the temperature of the joint is increased by this cross-heating. The temperature increase due to coil current during the latching process is therefore of the utmost importance. The electromagnetic force is linear to the LM current whereas the temperature is proportional to the square of this current. Since the temperature of the SMP need to be kept below its glass transition to avoid undesired softening, the maximum magnetic force is limited by the glass transition temperature of the chosen SMP material. Using an SMP with higher glass transition temperature allows higher electromagnetic force.

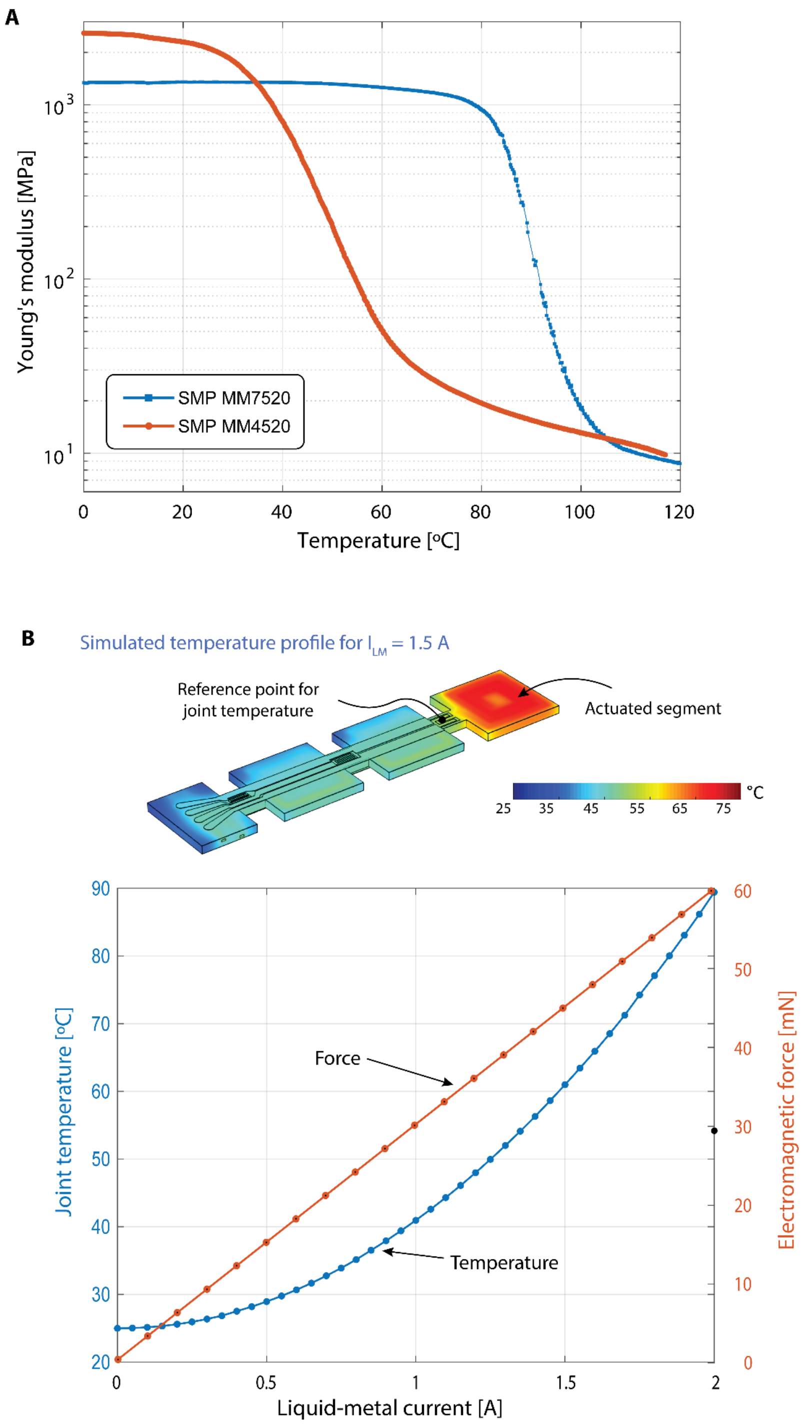

Fig. S7. The selection of the SMP material. (**A**) The Young's moduli of two different SMP materials are plotted as functions of the temperature. MM4520 and MM7520 are thermoplastic polyurethanes with glass transition temperatures around 45 °C and 80 °C, respectively. (**B**) The electromagnetic force and the temperature of the adjacent joint as functions of the LM current. The electromagnetic force is linear to the LM current whereas the temperature of the adjacent joint is proportional to the square of the current. The temperature is simulated using a finite element model (COMSOL) and the electromagnetic force is numerically calculated by assuming the magnet and the coil as two magnetic dipoles. As MM4520 gets soft at lower temperature, the maximum electromagnetic force of this materials is around 30 mN, whereas with high T_g SMP, which allows operation at higher LM current and therefore higher electromagnetic force is achievable.

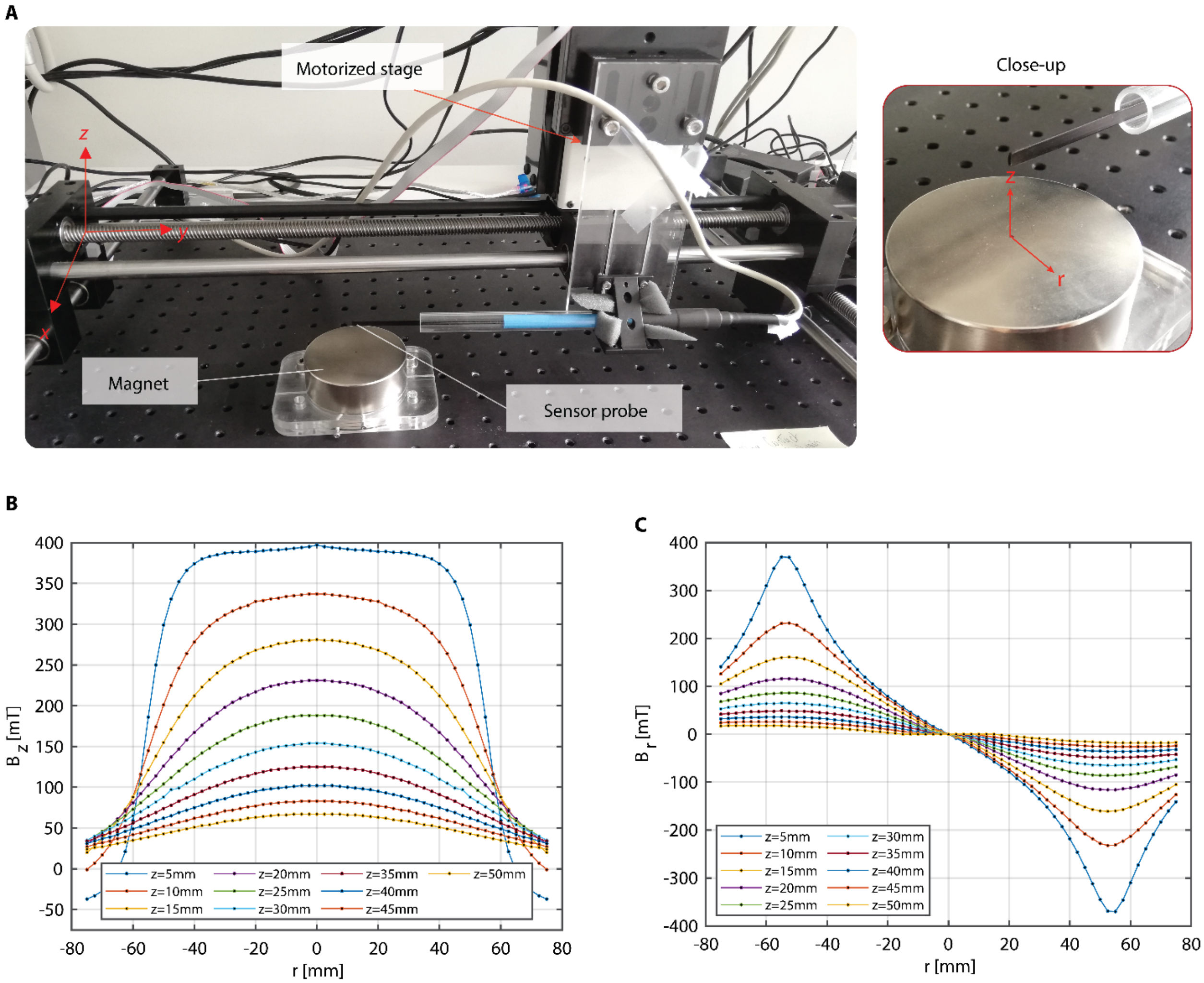

Fig. S8: Characterization of the plate magnet. (**A**) The setup used for the magnetic field measurement. The magnet has a radius of 35 mm and a height of 35 mm. The magnetic field was measured using a Teslameter (Gauss-Teslameters FH55 from Magnet-Physik). The sensor probe was attached to a motorized XYZ state. The magnetic field in radial $B_{r(z,r)}$ and axial $B_{z(z,r)}$ directions were measured as functions of z and r. (**B**) Measured magnetic field in the axial direction as function of the radius for different heights. This measured magnetic field was used in our calculations. (**C**) Measured magnetic field in the radial direction at different heights.

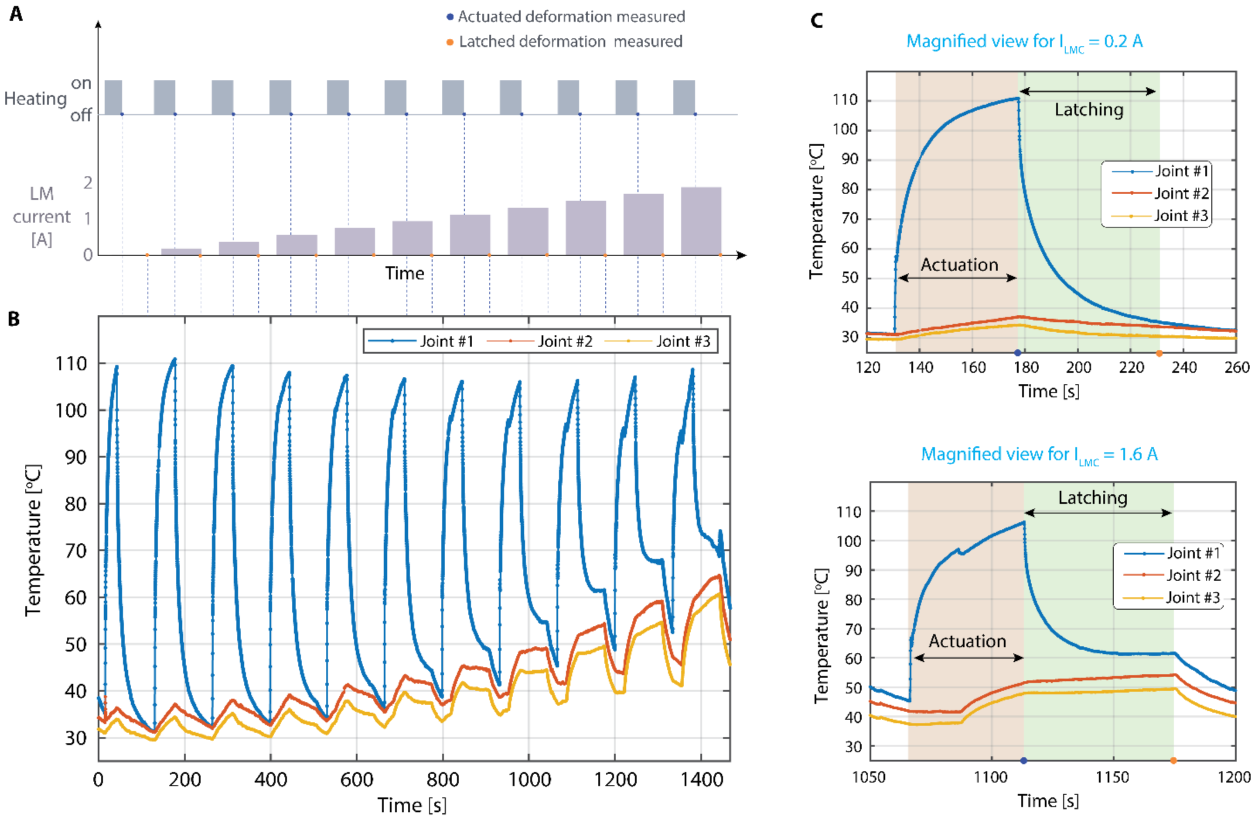

Fig. S9. Time evolution of the temperature of the joints during actuator characterization. The temperature was measured in the middle of each joint using an IR camera. (**A**) Time sequence of the voltage applied to the heaters and of the current driven in the liquid-metal coils (LM current). The LM current was increased from 0 A to 2 A with an increment of 0.2 A. For each LM current increment, the device is actuated, the shape is then fixed, and finally the initial flat shape is recovered by heating the joint. (**B**) The temperature of the joints is plotted as a function of time as the joint #1 is heated and actuated at different LM currents. (**C**) The magnified views of the joints temperature at low (0.2 A) and high (1.6 A) LM currents.

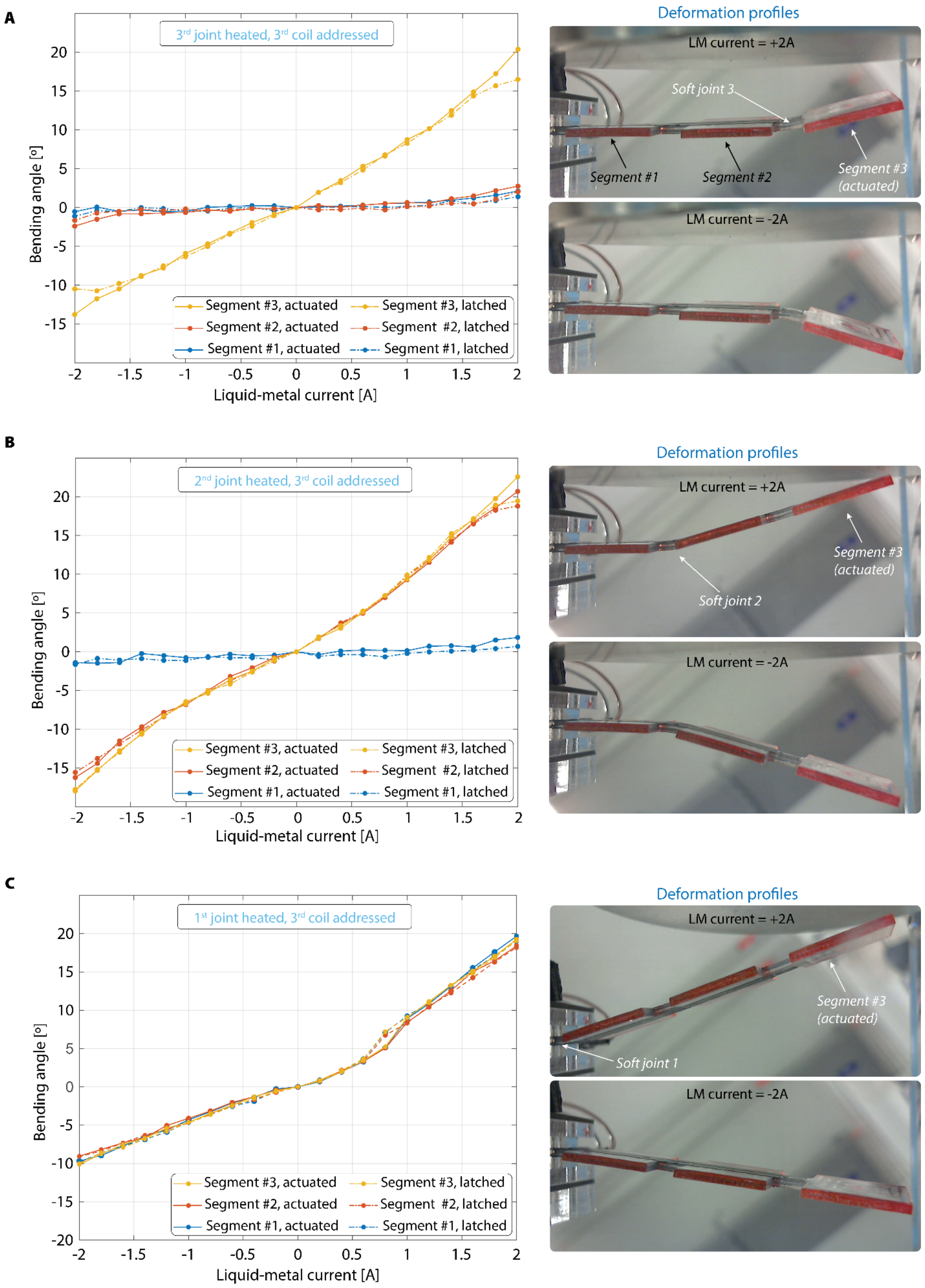
A
3rd joint heated, 3rd coil addressed
Bending angle [º]
20
15
10
5
0
-5
-10
-15
-2
-1.5
-1
-0.5
0
0.5
1
1.5
2
Liquid-metal current [A]
Segment #3, actuated
Segment #3, latched
Segment #2, actuated
Segment #2, latched
Segment #1, actuated
Segment #1, latched
Deformation profiles
LM current = +2A
Soft joint 3
Segment #1
Segment #2
Segment #3 (actuated)
LM current = -2A
B
2nd joint heated, 3rd coil addressed
Bending angle [º]
20
15
10
5
0
-5
-10
-15
-2
-1.5
-1
-0.5
0
0.5
1
1.5
2
Liquid-metal current [A]
Segment #3, actuated
Segment #3, latched
Segment #2, actuated
Segment #2, latched
Segment #1, actuated
Segment #1, latched
Deformation profiles
LM current = +2A
Segment #3 (actuated)
Soft joint 2
LM current = -2A
C
1st joint heated, 3rd coil addressed
Bending angle [º]
20
15
10
5
0
-5
-10
-15
-20
-2
-1.5
-1
-0.5
0
0.5
1
1.5
2
Liquid-metal current [A]
Segment #3, actuated
Segment #3, latched
Segment #2, actuated
Segment #2, latched
Segment #1, actuated
Segment #1, latched
Deformation profiles
LM current = +2A
Segment #3 (actuated)
Soft joint 1
LM current = -2A

Fig. S10. Experimental results showing the bending and latching of the joints. (**A**) The deflection angle of the segments is plotted as function of the LM current when the first joint was softened and the first segment was actuated. The segment approached to the magnet when a positive current is applied to the LM coil and moved away from the magnet for the negative LMC current. The deformation in the approaching cases was higher due to the higher magnetic field. The unaddressed joints were very stiff and therefore had very small deformation. The joint had high shape fixation for LM current <1.5 A and slightly decreases above 1.5 A of the LM current. (**B**) The graph shows the deflection angle of the segments when the second joint was softened and the first segment was actuated. Actuating the first segment instead of the second segment increases the distance between the electromagnetic force and the soft joints, resulting higher bending moment and therefore higher deformation. As the joint between the 1st and 2nd segments were stiff, they moved together with the same deflection angle. (**C**) When the third joint (the joint between the last segment and the clamps) was softened, the device acted as a rigid beam with a deformable section closed to the clamps. All segment had the same deflection angle as the joints between them are rigid. Due to the variation among their widths and the heat distribution during the actuation, the joints had different deformations.

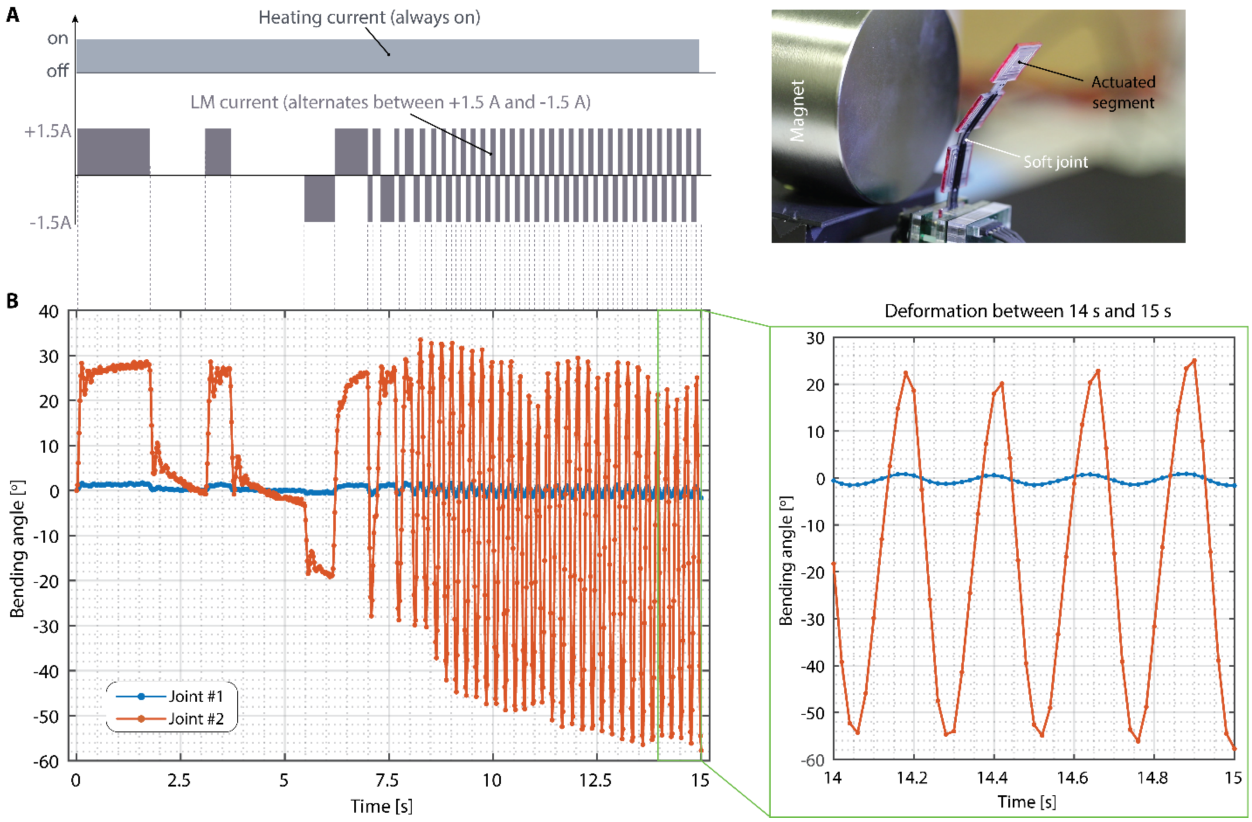

Fig. S11. The response of a joint in the hot state at up to 4 Hz actuation. The video of this experiment is shown in supplementary Movie S1. (**A**) Time sequence of the heating currents and liquid-metal (LM) currents. During this experiment, the heater of the 2nd joint was kept on while the LM current in segment #3 was switched between +1.5 A and -1.5 A. The soft joint and actuated segment are shown in the photograph. (**B**) The bending deformation of the soft (red line) and rigid (blue line) joints vs time as the LM current is changed. The right-side zoom shows the response to a 4 Hz drive, showing fast deformation at large amplitude. The device could respond faster if driven at higher frequencies.

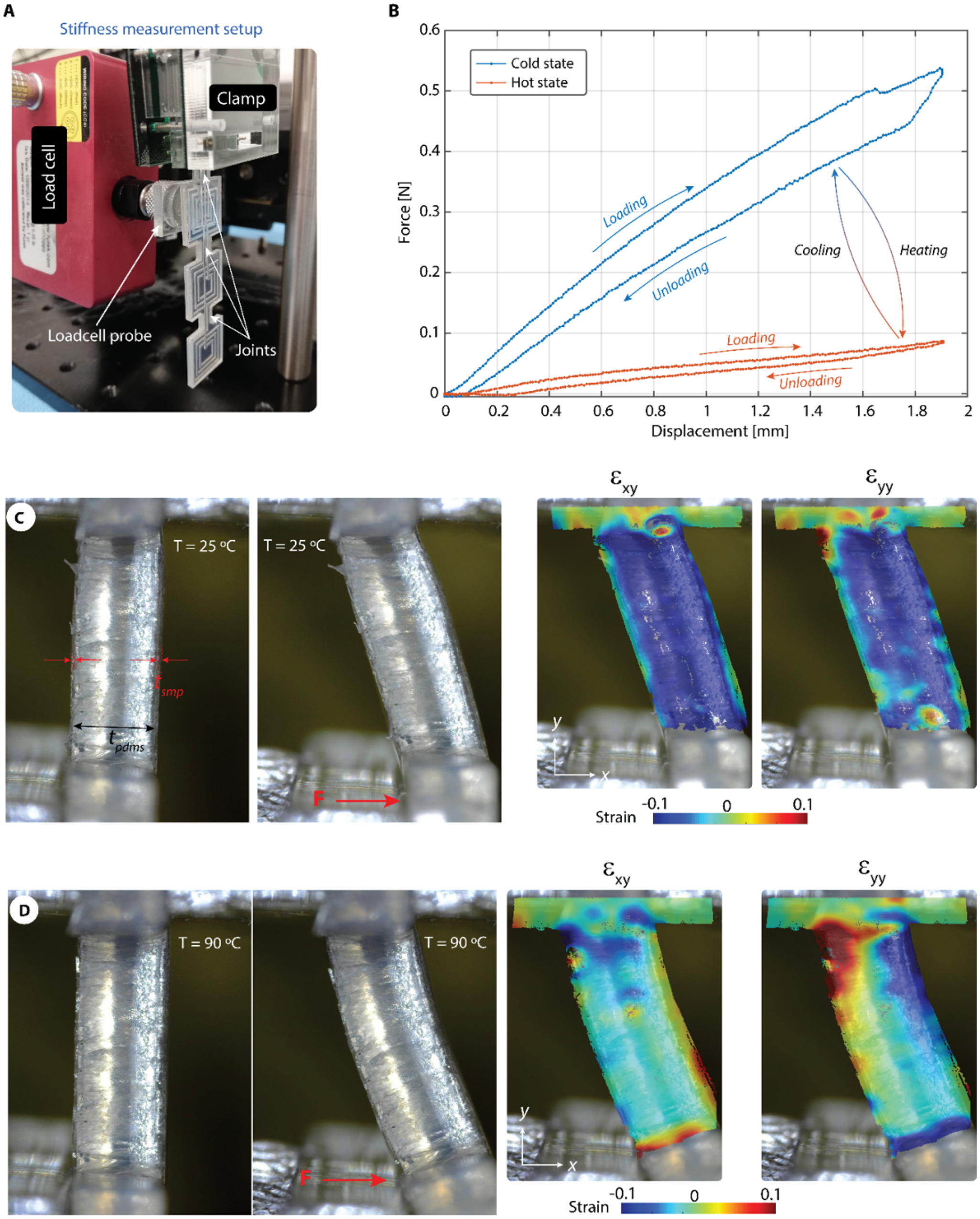

Fig. S12. The stiffness measurement of the joints and their deformation analysis at the room and elevated (90 °C) temperatures. (**A**) The experimental setup used to measure the bending stiffness of the joints. (**B**) Measured bending stiffness of a joint at 25 °C and 90 °C, corresponding the temperatures in the actuated and latched states. The bending stiffness of the joint at room temperature is approximately 7 times higher than at 90 °C. (**C-D**) The micrographs show the side view of the joint as it is deformed at the room temperature. The region in focus is the side view of the joint whereas the clamp and the tip of the load cell are not in the field of view. The joint was clamped from the top edge and the displacement was applied to the bottom edge. At room temperature, the joint undergoes a shear deformation whereas at 90 °C the joint has a bending deformation. The strain components are mapped on the deformed images to compare their deformation at different temperatures. At room temperature, the SMP layers has smaller strains (ε_{xx} and ε_{yy}) than the PDMS layers, indicating the large deformation occurs in the PDMS layer. At 90 °C, the SMP layers are very soft (easy to deform them) and the joint undergoes a bending deformation where the SMP layers has the highest tensile and compressive strains.

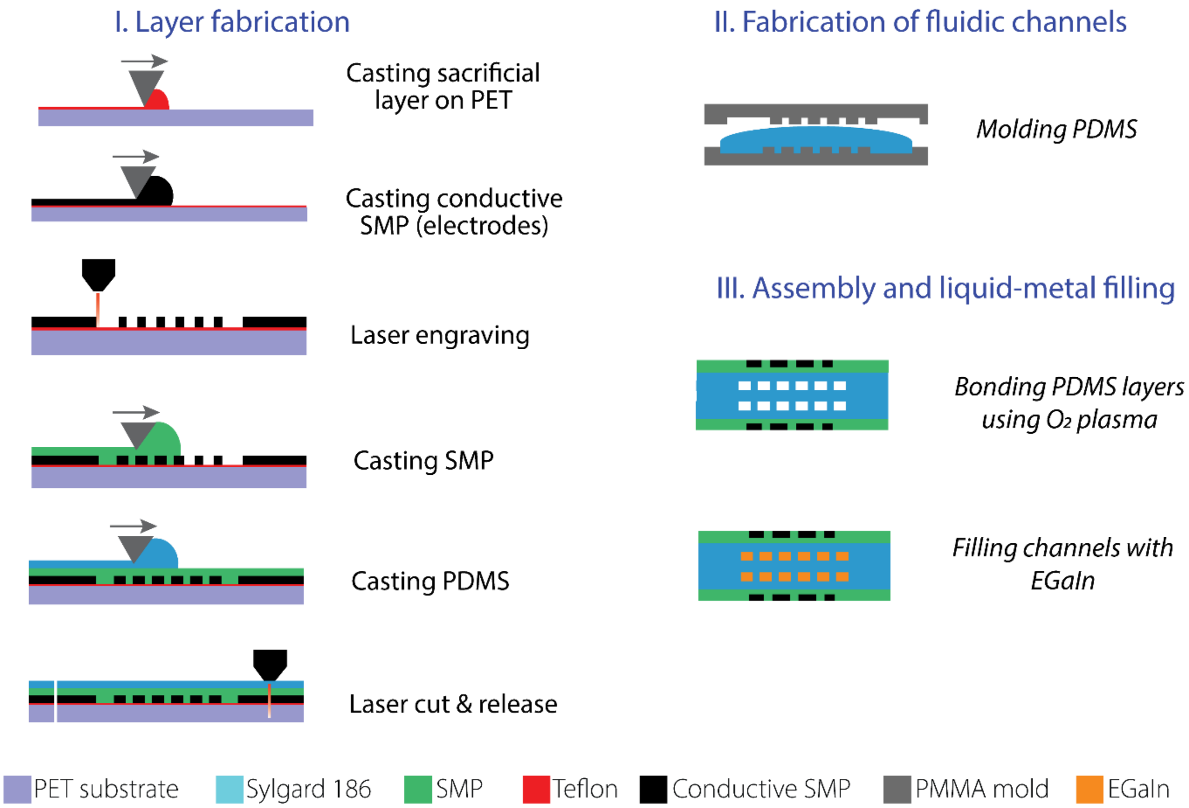

Fig. S13. Fabrication process flow. The fabrication starts with casting of multilayer of conductive SMP, SMP, PDMS, and a sacrificial layer of Teflon on a PET substrate. Two PMMA master molds are used to fabricate silicone microfluidic channels. The PDMS solution is poured into the PMMA molds and clamped, and cured in the oven at 80 °C for 1 h. Two layers of PDMS+SMP composite are bonded on both sides of the molded PDMS using oxygen plasma treatment. An acrylic based conductive type is patterned with laser cutter and is placed on the top and on the bottom of the assembled structure. Finally, the PDMS channels are filled with EGaIn using a syringe.

Movie S1.

Variable stiffness electromagnetically actuated structure, showing the selective actuation and latching of the three segments. Each segment can individually deform (twist or bend) and then lock in the deformed shape.

Movie S2.

Demonstrations of the device in several scenarios, going through a series of local deformations and shape fixation steps: Grasping and holding objects (up to 2.5 N), matching a slit orientation in a tip-tilt stage, and the insertion of an initially flat device through a series of differently oriented slits.